

RESEARCH ARTICLE

Reaction Engineering, Kinetics and Catalysis

Plasma-driven CO₂ hydrogenation to CH₃OH over Fe₂O₃/γ-Al₂O₃ catalystShengyan Meng¹ | Liang Wu² | Miao Liu¹ | Zhaolun Cui³ | Qian Chen¹ |
Shangkun Li^{1,4} | Jiahui Yan¹ | Li Wang⁵ | Xinkui Wang¹ | Ji Qian¹ |
Hongchen Guo¹ | Jinhai Niu² | Annemie Bogaerts⁴ | Yanhui Yi¹ ¹State Key Laboratory of Fine Chemicals, School of Chemical Engineering, Dalian University of Technology, Dalian, China²Liaoning Key Lab of Optoelectronic Films and Materials, School of Physics and Materials Engineering, Dalian Nationalities University, Dalian, China³School of Electric Power Engineering, South China University of Technology, Guangzhou, China⁴Research group PLASMANT, Department of Chemistry, University of Antwerp, Antwerp, Belgium⁵College of Environmental Sciences and Engineering, Dalian Maritime University, Dalian, Liaoning, China

Correspondence

Jinhai Niu, Liaoning Key Lab of Optoelectronic Films and Materials, School of Physics and Materials Engineering, Dalian Nationalities University, Dalian, 116600 China.
Email: niujh@dlnu.edu.cnYanhui Yi, State Key Laboratory of Fine Chemicals, School of Chemical Engineering, Dalian University of Technology, Dalian 116024, China.
Email: yianhui@dlut.edu.cn

Funding information

Fundamental Research Funds for the Central Universities of China, Grant/Award Number: DUT18JC42; National Natural Science Foundation of China, Grant/Award Numbers: 21908016, 21978032

Abstract

We report a plasma-assisted CO₂ hydrogenation to CH₃OH over Fe₂O₃/γ-Al₂O₃ catalysts, achieving 12% CO₂ conversion and 58% CH₃OH selectivity at a temperature of nearly 80°C atm pressure. We investigated the effect of various supports and loadings of the Fe-based catalysts, as well as optimized reaction conditions. We characterized catalysts by X-ray powder diffraction (XRD), hydrogen temperature programmed reduction (H₂-TPR), CO₂ and CO temperature programmed desorption (CO₂/CO-TPD), high-resolution transmission electron microscopy (HRTEM), scanning transmission electron microscopy (STEM), x-ray photoelectron spectroscopy (XPS), Mössbauer, and Fourier transform infrared (FTIR). The XPS results show that the enhanced CO₂ conversion and CH₃OH selectivity are attributed to the chemisorbed oxygen species on Fe₂O₃/γ-Al₂O₃. Furthermore, the diffuse reflectance infrared Fourier transform spectroscopy (DRIFTS) and TPD results illustrate that the catalysts with stronger CO₂ adsorption capacity exhibit a higher reaction performance. *In situ* DRIFTS gain insight into the specific reaction pathways in the CO₂/H₂ plasma. This study reveals the role of chemisorbed oxygen species as a key intermediate, and inspires to design highly efficient catalysts and expand the catalytic systems for CO₂ hydrogenation to CH₃OH.

KEYWORDS

chemisorbed oxygen, CO₂ hydrogenation, iron-based catalyst, methanol production, plasma catalysis

1 | INTRODUCTION

The increased concentration of CO₂ results in significant environmental impacts, such as global warming and sea level rise.¹ To effectively control the greenhouse effect caused by CO₂, there is an urgent need for CO₂ emission reduction. Currently, carbon capture and storage

(CCS) or utilization (CCU) are the main strategies to mitigate CO₂ emissions.^{2,3} Obviously, compared to CCS, CCU can not only reduce CO₂ emissions but also produce value-added chemicals (e.g., CO, CH₄, CH₃OH, DME, and higher hydrocarbons). Among these chemicals, CH₃OH is an important industrial chemical, since it is used as a gasoline additive, a hydrogen storage compound, and a feedstock for the

production of bulk chemicals (e.g., olefins and aromatics). Therefore, the production of CH₃OH through hydrogenation of CO₂ has attracted major attention of researchers. However, based on Le Chatelier's principle, a considerable CH₃OH selectivity can only be achieved at high pressure. That is, caused by thermodynamic limitations and a kinetic barrier, usually 2–5 MPa and 180–330°C have been adopted in CO₂ hydrogenation to CH₃OH.^{4–8}

The combination of catalysts and nonthermal plasma (NTP), in so-called plasma catalysis, is a potential strategy to realize CO₂ hydrogenation to CH₃OH at mild conditions. In NTP, the overall gas temperature typically remains below 100°C, while the generated electrons are highly energetic, with a typical temperature of 1–10 eV, which is sufficient to activate reactant molecules (e.g., CO₂ and H₂) into radicals, excited atoms and molecules, and ions. These reactive species can initiate a variety of chemical reactions at room temperature.^{9–11}

In recent years, plasma-catalytic CO₂ hydrogenation has attracted more and more attention, but mainly focused on the reverse water gas shift (RWGS) reaction^{12–15} and the methanation reaction.^{16–21} Plasma-catalytic CO₂ hydrogenation for methanol synthesis is a promising process for CO₂ conversion and utilization.²² In our previous work, we achieved 54% CH₃OH selectivity over Cu/ γ -Al₂O₃ catalyst.²³ Recently, we revealed the reaction mechanism of CH₃OH production over Cu/ γ -Al₂O₃ catalyst at ambient temperature by combing experimental results and DFT calculations.²⁴

In-, Mo-, Ni-, and Cu-based catalysts have been reported to have good catalytic properties in CO₂ hydrogenation to methanol.^{25–30} Fe-based catalysts have been reported to have good catalytic properties in CO₂ hydrogenation to hydrocarbons,³¹ and Co-based catalysts can promote the C–C coupling reaction.³² Therefore, in this work, we investigated the catalytic performance of CoO, In₂O₃, MoO₃, NiO, CuO, and Fe₂O₃ in plasma-catalytic CO₂ hydrogenation to CH₃OH, and the Fe₂O₃/ γ -Al₂O₃ catalyst shows the best CH₃OH selectivity (58%) and CO₂ conversion (12%), operated at atmospheric pressure and 80°C. Our characterization results show that the catalyst with more chemisorbed oxygen species, as well as stronger CO₂ adsorption capacity, exhibits a higher CO₂ conversion and CH₃OH selectivity. Fe-based catalysts are usually used in CO₂ hydrogenation for production of hydrocarbons.^{31,33} Although very few papers report the catalysis of Fe₂O₃ species for CO₂ hydrogenation to CH₃OH, it often needs to combine with another component.^{34,35} Vajda et al. described a Cu₄/Fe₂O₃ catalyst for CO₂ hydrogenation to methanol at near atmospheric pressure.³⁴ They found that Cu₄ clusters facilitate the reduction of Fe₂O₃-producing surface-rich Fe²⁺ species in the proximate sites, and the as-formed Fe²⁺ species in return promote CO₂ activation and transformation over Cu₄ cluster. Loganathan et al. reported a quartz wool-supported CuO–Fe₂O₃ catalyst for CO₂ hydrogenation to CH₃OH, by combining thermal catalysis and NTP with an input power of 2 W, achieving 16.7% CO₂ conversion with 32.7% CH₃OH selectivity.³⁵ Noted that Xie et al. studied methanol/ethanol synthesis using a Fe₂O₃/Al₂O₃ catalyst and a slurry reactor, but they used syngas (CO/H₂ mixture) as a feed stock.³⁶ Therefore, our paper is very useful to expand the catalytic systems, focusing on the role of chemisorbed oxygen species, for CO₂ hydrogenation to CH₃OH.

2 | EXPERIMENTAL

2.1 | Catalyst preparation

Fe₂O₃/ γ -Al₂O₃ catalysts with various loadings (i.e., 1, 3, 5, 10, 20, and 25 wt.%) were prepared by incipient wetness impregnation. High-purity γ -Al₂O₃ (Dalian Luming Nanometer Material Co., Ltd., and the water absorption of γ -Al₂O₃ support is 1.25 mL/g) was used as support, which was calcined in air at 350°C for 5 h before the addition of metal precursor solution. The concentrations of the aqueous solutions of metal precursors were adjusted at room temperature to obtain the appropriate Fe loading on the final catalysts. The impregnated samples were dried overnight in air at 120°C. After cooling to room temperature, the samples were calcined in a muffle furnace for 5 h at 450°C. Finally, the catalysts (20–40 mesh) prepared by incipient wetness impregnation were stored in a closed container before use.

Iron-based catalysts using different supports, that is, SiO₂, TiO₂, CeO₂, In₂O₃, ZrO₂, and Al(OH)₃, were also prepared with 5 wt.% loading via the same incipient wetness impregnation method, and the obtained samples are denoted as Fe₂O₃/SiO₂, Fe₂O₃/TiO₂, Fe₂O₃/CeO₂, Fe₂O₃/In₂O₃, Fe₂O₃/ZrO₂, and Fe₂O₃/Al(OH)₃, respectively. Finally, the same method was used to prepare other catalysts with different active metals, that is, CoO/ γ -Al₂O₃, In₂O₃/ γ -Al₂O₃, MoO₃/ γ -Al₂O₃, NiO/ γ -Al₂O₃ and CuO/ γ -Al₂O₃.

2.2 | Catalytic tests

The hydrogenation of CO₂ to CH₃OH at atmospheric pressure was carried out using the plasma catalysis set up illustrated in Figure S1. A dielectric barrier discharge (DBD) reactor with a liquid grounding electrode (water) and a metal high-voltage electrode (stainless steel rod) was designed. The discharge length of the DBD reactor was fixed at 50 mm with a discharge gap of 4 mm, and 1.2 g catalyst was packed into the discharge area. The flow rate of CO₂ and H₂ was maintained at 18 and 57 mL/min, respectively, by mass flow controllers. Typically, the temperature of the circulating water (grounding electrode) was maintained at 60°C, the discharge frequency was fixed at 9 kHz, and the effective discharge power was fixed at 18 W (calculated by the Q-U Lissajous method). The change of gas volume was measured by soap film meters. The temperature of the discharge area was measured with an infrared camera, as shown in Figure S2. It can be seen that the temperature of the inner reactor wall was around 60°C, which is similar to the temperature of the circulating water (the grounding electrode). However, the temperature of the central area of the catalyst bed was around 80°C, which is caused by the exothermal character of CO₂ hydrogenation and by the high energy density of the DBD plasma. Moreover, the waveforms of discharge voltage and current were measured by a four-channel digital oscilloscope (Tektronix, DPO 3012), equipped with a high-voltage probe (Tektronix P6015A) and a current probe (Pearson 6585). A cold trap (i.e., mixture of liquid nitrogen and acetone) was placed at the exit of the DBD reactor to condense liquid products.

The tail gas was analyzed using a gas chromatograph equipped with a thermal conductivity detector (TCD) of Tianmei 7890 II. The exact flow rate of tail gas before and after the reaction was measured via a flow meter, to eliminate the analysis error caused by gas compression/expansion. The liquid oxygenate products (collected in the cold trap) were quantitatively analyzed using a gas chromatograph (Shimadzu GC-2014) equipped with a flame ionization detector (FID) and a PEG-20 M column. Gas products were injected into a gas chromatograph (Tianmei 7890 II) equipped with a TCD and a TDX-01 column online every 30 min, and the liquid products were detected after a 3 h reaction. The signal value of exhaust gas was analyzed online by a mass spectrometer (HIDEN) with Faraday detection mode.

To evaluate the reaction performance of the catalyst, the CO₂ conversion (X) and selectivity (S) of the major products were calculated via the following formulas. It is worth noting that, in the condensed liquid, only CH₃OH has been detected. In the tail gas, besides CH₄ and CO, also unreacted CO₂ and H₂ were detected (Figure S3). Also, there was no carbon deposition (coking) in the catalyst after the reaction. Therefore, CO, CH₄, and CH₃OH are the only products in our experiments, and thus, the selectivity of CH₃OH can be reasonably calculated using Formula (4). Furthermore, we checked the carbon balance, and it is close to 100% in the case of 20 h continuous operation (Figure S4). The energy consumption of CH₃OH formation (J/mol) is defined by Formula (5).

$$X_{\text{CO}_2}(\%) = \frac{n(\text{CO}_2)_{\text{in}} - n(\text{CO}_2)_{\text{out}}}{n(\text{CO}_2)_{\text{in}}} \times 100\% \quad (1)$$

$$S_{\text{CO}}(\%) = \frac{n(\text{CO})_{\text{out}}}{n(\text{CO}_2)_{\text{in}} - n(\text{CO}_2)_{\text{out}}} \times 100\% \quad (2)$$

$$S_{\text{CH}_4}(\%) = \frac{n(\text{CH}_4)_{\text{out}}}{n(\text{CO}_2)_{\text{in}} - n(\text{CO}_2)_{\text{out}}} \times 100\% \quad (3)$$

$$S_{\text{CH}_3\text{OH}}(\%) = 100\% - S_{\text{CO}} - S_{\text{CH}_4} \quad (4)$$

$$\text{energy consumption (kJ/mmol)} = \frac{\text{discharge power (J/s)}}{\text{rate of CH}_3\text{OH produced (mol/s)} \times 10^{-6}} \quad (5)$$

2.3 | Catalyst characterization

The crystalline structure of the catalysts was determined by x-ray powder diffraction (XRD) using an x-ray diffractometer (Rigaku D-Max 2400) with Cu K α radiation ($\lambda = 0.15406$ nm). For ⁵⁷Fe Mössbauer measurements, the samples were recorded on an MFD-500AV spectrometer at room temperature. ⁵⁷Co (Rh) was used as a radioactive source, and α -Fe was used as reference at 25°C. Nitrogen adsorption-desorption isotherms of the samples were obtained at -196°C using a N₂ physisorption apparatus (Micromeritics ASAP 3020). The specific surface area was calculated using the Brunauer-Emmett-Teller (BET) method. The total pore volume (V_p) was determined at a relative pressure of $P/P_0 = 0.99$, and the mean pore

diameter (D_p) was determined by the Barret-Joyner-Halenda (BJH) method from the desorption branch of the isotherm. Microstructure characterization of the catalysts was examined by high-resolution transmission electron microscopy (HRTEM) (Tecnai G2 F30 S-Twin), with an energy dispersive x-ray spectrometer (EDXS) and scanning transmission electron microscopy (STEM) with bright field (BF) and dark field (DF), at an accelerating voltage of 300 kV. X-ray photoelectron spectroscopy (XPS) was carried out using a Thermo ESCALAB XI + spectrometer to reveal the valence states and chemical environment of the elements in the catalysts.

The redox behavior of the fresh and spent catalysts was investigated by hydrogen temperature programmed reduction (H₂-TPR) using a chemisorption instrument (Quantachrome ChemBET 3000). The TPR analysis was carried out in an H₂/Ar mixture flow (10% H₂, 120 cm³/min) from room temperature to 800°C with a heating rate of 10°C/min. The H₂ concentration in the tail gas was monitored by the TCD, to indicate the H₂ consumption as a function of temperature. CO₂ and CO temperature programmed desorption (CO₂/CO-TPD) were performed at the same apparatus. The sample was then purged with CO₂ or CO for another 1 h at 30°C. Helium purging was followed to remove CO₂ or CO, which was physically adsorbed on the catalyst. Finally, the sample was heated to 700°C under the flowing helium. The composition of the effluent gas was measured by the TCD. Diffuse reflectance infrared Fourier transform spectroscopy (DRIFTS) was executed on a Fourier transform infrared spectrometer (Nicolet 6700) equipped with mercury-cadmium-telluride detector (cooled by liquid nitrogen) by averaging 64 scans at resolution of 8 cm⁻¹ in the range of 4000-400 cm⁻¹. The DRIFTS cell (Harrick, HVC-DRP) fitted with ZnSe windows was used as the reaction chamber. For all of the DRIFTS experiments, the catalysts were first purged with N₂ at 400°C for 240 min, and the flow rate was controlled at 40 mL min⁻¹. Subsequently, the catalysts were exposed to CO₂ flow (20 mL min⁻¹) at 25°C for 30 min. After that, the atmosphere was switched to N₂ (40 mL min⁻¹), aiming to purge CO₂ adsorbed on the catalyst. Finally, the DRIFTS were collected.

2.4 | Plasma diagnostics

The emission spectra of the H₂/CO₂ plasma at different conditions were recorded using a Princeton Instruments ICCD spectrometer (SP 2758) in the range of 200-1200 nm via an optical fiber, which directly faces toward the outside wall of the DBD reactor. The slit width and grating of the spectrometer were fixed at 20 μ m and 300 g mm⁻¹, respectively.

3 | RESULTS AND DISCUSSION

3.1 | Catalytic performance

As shown in Figure S5a,c, among the different metal oxide catalysts, Fe₂O₃/ γ -Al₂O₃ shows the highest CH₃OH selectivity (ca. 58%) and

CO₂ conversion (ca. 12%). In addition, the effect of various supports was also investigated using Fe as the loading metal. As shown in Figure S5b,d, the catalyst with γ -Al₂O₃ as support, that is, Fe₂O₃/ γ -Al₂O₃, exhibits the best catalytic performance. Furthermore, the residence time of the CO₂/H₂ mixture, the mole ratio of CO₂/H₂, the discharge power, and the temperature of circulating water were also investigated, and the results are presented in Figure 1 and Table S1.

The variation of residence time was realized by adjusting the flow rate of CO₂/H₂ mixture (Figure 1A). The specific energy input (SEI) was different when we investigated the effect of residence time on the reaction performance. The longer the residence time, the higher the SEI. For chemical reaction driven by plasma, usually, high SEI favors endothermic reaction, but restrain exothermic reaction, since high SEI leads to a strong heating effect (Figure S6).^{37,38} More importantly, the longer residence time may lead to higher probability of collisions between energetic electrons and reactive species, which would further affect the products distributions. That is, CH₃OH decomposition caused by collisions with energetic electrons may be the main

reason why we achieved a low CH₃OH selectivity at longer residence time, compared with 3.1 s. On the other hand, the shorter residence time also seems inappropriate because CO₂ hydrogenation is a step-wise process, which means that production of CH₃OH from CO₂ hydrogenation needs many elementary reaction steps. Therefore, a moderate residence time (3.1 s) is necessary in this study. As shown in Figure 1B, there is no significant difference in methanol selectivity at different CO₂/H₂ molar ratios. However, higher CO₂ conversion was obtained in the case of lower CO₂/H₂ molar ratio.

As shown in Figure 1C, the higher the input power, the higher the CO₂ conversion, which is mainly due to the higher density of energetic electrons promoting the dissociation of CO₂. However, the CH₃OH selectivity decreased but CO selectivity increased with the increasing of input power, which means that higher input power can promote RWGS reaction but inhibit CH₃OH synthesis, and the decomposition of methanol will also take place under the high input power. In this work, we used a critical discharge power of ca. 18 W (the lowest power to trigger the discharge) for the subsequent

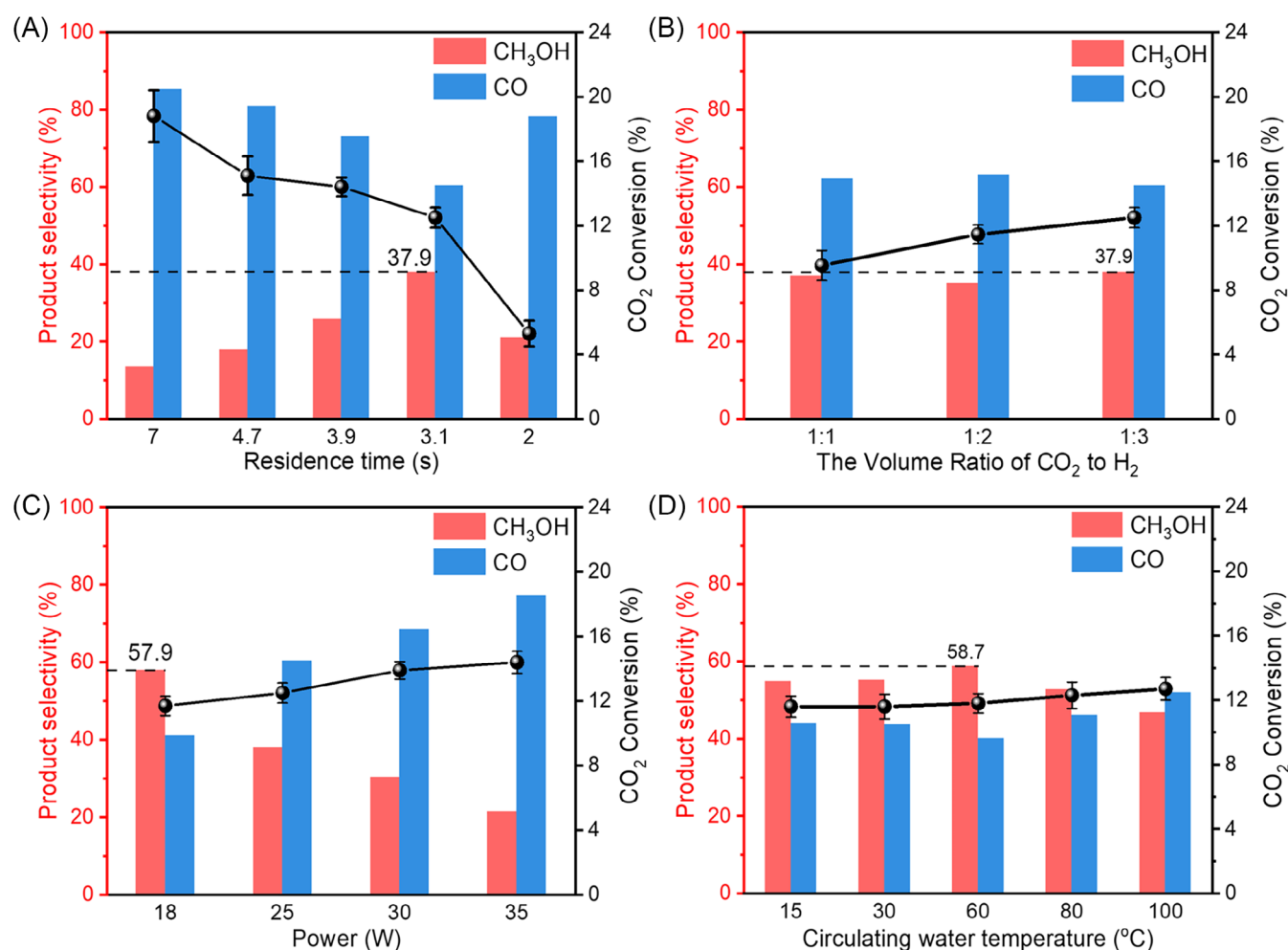


FIGURE 1 CO and CH₃OH selectivity and CO₂ conversion at different plasma catalysis conditions. (A) Effect of residence time, at discharge power 25 W, CO₂/H₂ = 1/3, 60°C circulating water; (B) Effect of CO₂/H₂ ratio, at discharge power 25 W, residence time 3.1 s, 60°C circulating water; (C) Effect of input power, at CO₂/H₂ = 1/3, residence time 3.1 s, 60°C circulating water. (D) Effect of circulating water temperature, at discharge power 18 W, CO₂/H₂ = 1/3, residence time 3.1 s. (discharge frequency 9 kHz, 1 atm pressure).

plasma-catalytic reaction. The products distribution was also regulated by changing the temperature of circulating water, as shown in Figure 1D. It can be seen that the optimized temperature of circulating water for CO₂ hydrogenation to CH₃OH is ca. 60°C. In this case, the average temperature in the discharge area is about 80°C (Figure S2), which is slightly higher than the boiling point of CH₃OH (64.8°C). Thus, we suggest that this temperature may favor desorption of CH₃OH during plasma-catalytic CO₂ hydrogenation since desorption of CH₃OH usually needs to overcome an energy barrier.²⁴ The lower temperature of circulating water (15°C and 30°C), however, may inhibit the desorption of CH₃OH, and the higher temperature of circulating water (80°C and 100°C) may promote the RWGS reaction,^{12–15} which could be another reason why moderate temperature (60°C) is favorable for plasma-catalytic CO₂ hydrogenation to produce CH₃OH.

Different loadings of the Fe₂O₃/γ-Al₂O₃ catalysts were also investigated under the optimized reaction conditions. As shown in Figure 2A, the CO₂ conversion and CH₃OH selectivity show a volcano curve with increasing Fe loading, and the best performance was achieved at 5 wt.% loading, indicating that a modest loading is beneficial to plasma-catalytic CO₂ hydrogenation to CH₃OH.

In Figure 2B, we compare the CO₂ conversion and product selectivity for Fe₂O₃/γ-Al₂O₃ catalyst alone, plasma alone, plasma + γ-Al₂O₃ support, and plasma + Fe₂O₃/γ-Al₂O₃ catalyst. Obviously, the CO₂ conversion is zero without plasma, which means that the Fe₂O₃/

γ-Al₂O₃ catalyst cannot trigger the hydrogenation of CO₂ to CH₃OH under these conditions without the help of plasma. In the case of plasma + Fe₂O₃/γ-Al₂O₃, the CO₂ conversion and CH₃OH selectivity reach ca. 12% and 58%, respectively, which are much better than the results of plasma alone ($X_{\text{CO}_2} = 4.3\%$, $S_{\text{CH}_3\text{OH}} = 17\%$) and plasma + γ-Al₂O₃ ($X_{\text{CO}_2} = 8\%$, $S_{\text{CH}_3\text{OH}} = 24\%$). These results illustrate a significant synergistic effect between CO₂/H₂ plasma and Fe₂O₃/γ-Al₂O₃ catalyst for CH₃OH production, because the CO₂ conversion and CH₃OH selectivity are much higher than the sum of both individual processes. In addition, the selectivity of CH₄ remains at a low level under plasma conditions (<2%), which is consistent with our earlier studies.³⁹ Furthermore, as shown in Figure S7, the packing of quartz sand (negligible adsorption and hardly active sites) has been carried out for comparative experiments. It can be seen that quartz sand packing promotes CO₂ conversion and CO selectivity. This may be attributed to the increased field strength caused by quartz sand packing, which enhanced the discharge intensity, and thus lead to higher CO₂ conversion and CO selectivity (higher energy density favors RWGS reaction). This comparative experiment further demonstrates the catalytic role of Fe₂O₃/γ-Al₂O₃ in promoting CO₂ hydrogenation to CH₃OH through the adsorption of species on the active sites.

In addition, the energy consumption is dramatically reduced, as shown in Figure 2C. The energy consumption of plasma-catalytic CH₃OH production with Fe₂O₃/γ-Al₂O₃ catalyst is 19.8 kJ/mmol, which is much lower than plasma alone (181.7 kJ/mmol) and plasma

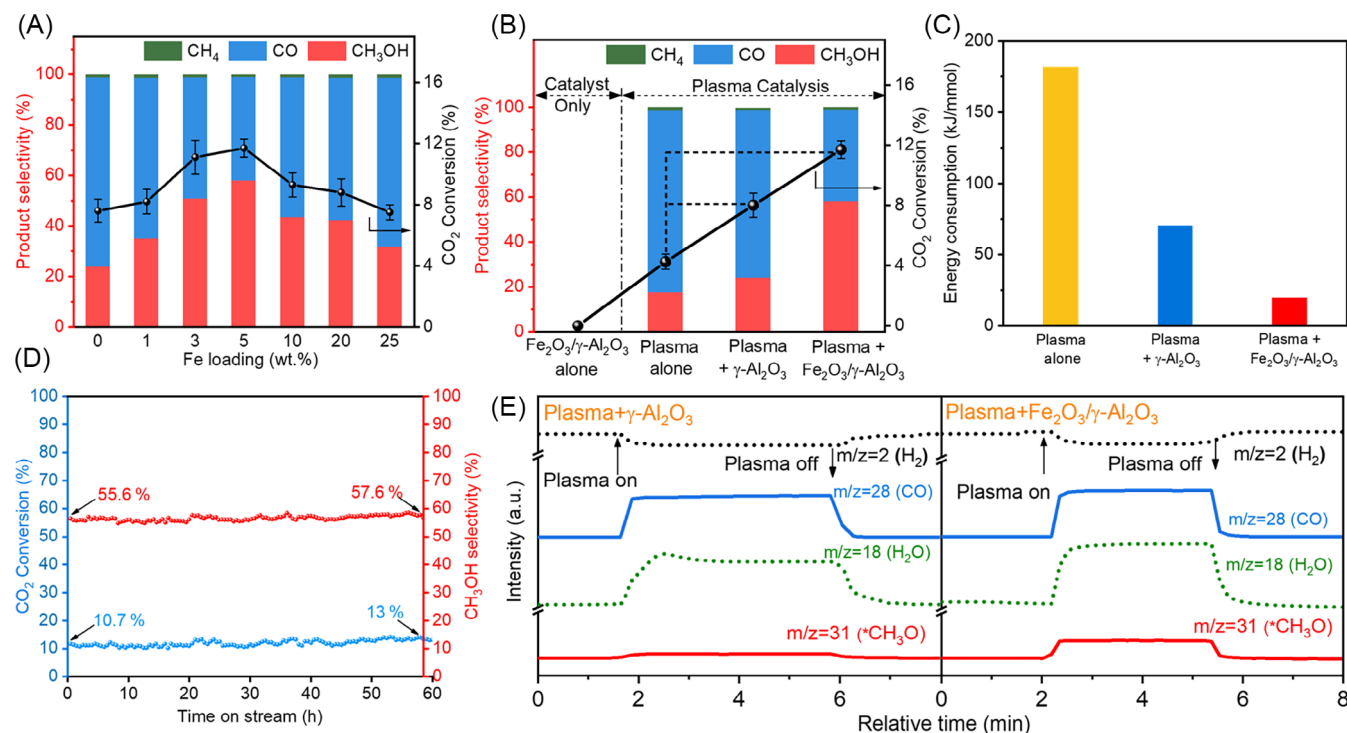


FIGURE 2 (A) Effect of various Fe loadings on CO₂ conversion and product selectivity; (B) Product selectivity and CO₂ conversion under different reaction conditions. (discharge power 18 W, discharge frequency 9 kHz, CO₂/H₂ = 1/3, residence time 3.1 s, 60°C circulating water, 1 atm pressure). (C) Energy consumption and CH₃OH concentration under different reaction conditions. (D) Stability test of Fe₂O₃/γ-Al₂O₃ catalyst in continuous operation for 60 h. (E) On-line MS analysis of product composition during reaction in the case of “plasma + γ-Al₂O₃” (left) and “plasma + Fe₂O₃/γ-Al₂O₃” (right).

+ γ - Al_2O_3 (70.5 kJ/mmol), indicating the key role of the Fe-based catalyst in improving the reaction performance.

We compare our results (for plasma catalysis) with some representative results from literature for conventional thermal catalysis, as shown in Table S2. Generally speaking, plasma catalysis experiments exhibit a similar degree of CO_2 conversion as conventional thermal catalysis, but the selectivity toward CH_3OH in our plasma catalysis experiments is a little lower than in conventional thermal catalysis, which is attributed to the high reactivity of the CO_2/H_2 plasma, leading also to production of CO through the RWGS reaction. However, conventional thermal catalysis generally needs to be operated at higher temperature (180–300°C) and higher pressure (0.5–36 MPa), while plasma catalysis can be operated at ambient temperature (typically below 100°C) and atmospheric pressure, which is the main advantage compared to conventional thermal catalysis. Furthermore, the energy consumption is also presented in Table S2, but since the data of conventional thermal catalysis are expressed in different units, we could not compare the energy consumption between plasma catalysis and thermal catalysis. Finally, the electrocatalytic CO_2 reduction reaction (CO_2RR) is also an attractive strategy because of recyclable electrolytes, modular systems, and high Faradaic efficiency. Both electrocatalysis and plasma catalysis rely on the use of renewable electrical energy and can be operated under mild conditions. The Faradaic efficiency of electrocatalysis (being a measure for the product selectivity) is a bit better than that of plasma catalysis. However, some challenges remain to be solved in electrocatalysis, such as the low solubility of CO_2 in aqueous solutions, the separation of product and electrolyte, and the instability of the electrode material.^{39–41}

Finally, during 60 h of continuous reaction, the CO_2 conversion and CH_3OH selectivity not only did not decrease, but gradually increased (X_{CO_2} from 10.7% to 13%, $S_{\text{CH}_3\text{OH}}$ from 55.6% to 57.6%), indicating that the $\text{Fe}_2\text{O}_3/\gamma\text{-Al}_2\text{O}_3$ catalyst has a relatively good catalytic stability, and the modification of $\text{Fe}_2\text{O}_3/\gamma\text{-Al}_2\text{O}_3$ catalyst by CO_2/H_2 plasma could be the reason for promoting CO_2 conversion and CH_3OH selectivity (Figure 2D).

The product composition was verified by on-line mass spectrometry (MS) from plasma-on to plasma-off in both the case of “plasma + $\gamma\text{-Al}_2\text{O}_3$ ” and “plasma + $\text{Fe}_2\text{O}_3/\gamma\text{-Al}_2\text{O}_3$ ”, as shown in Figure 2E. Clearly, compared to “plasma + $\gamma\text{-Al}_2\text{O}_3$,” the main fragmentation peak of $^*\text{CH}_3\text{O}$ ($m/z = 31$) show a significant increase in the case of “plasma + $\text{Fe}_2\text{O}_3/\gamma\text{-Al}_2\text{O}_3$.” This indicates that Fe_2O_3 plays a vital role in the production of CH_3OH , by providing the active sites for plasma-catalytic CO_2 hydrogenation to CH_3OH .

3.2 | Characterization of $\text{Fe}_2\text{O}_3/\gamma\text{-Al}_2\text{O}_3$ catalysts

Figure 3A shows the XRD patterns of the $\text{Fe}_2\text{O}_3/\gamma\text{-Al}_2\text{O}_3$ samples with various loading. No diffraction peaks of $\alpha\text{-Fe}_2\text{O}_3$ were observed when the loadings were below 5 wt.% (i.e., 1 and 3 wt.%), and the main diffraction peaks came from $\gamma\text{-Al}_2\text{O}_3$, indicating that Fe_2O_3 was highly dispersed on $\gamma\text{-Al}_2\text{O}_3$. However, diffraction peaks attributed to $\alpha\text{-Fe}_2\text{O}_3$ were observed (33.2°, 35.6°, 49.5°, 54.0°, 62.5°, and 64°)

when the loadings reached 5 wt.%. In addition, with the increase of Fe loading, the intensities of the main diffraction peaks increased, which means that the increasing Fe loading (5, 10, 20, and 25 wt.%) may lead to the aggregation of $\alpha\text{-Fe}_2\text{O}_3$ particles.⁴² Furthermore, the average particle size of Fe_2O_3 on $\gamma\text{-Al}_2\text{O}_3$ has been calculated using Scherrer formula, and then the dispersion of Fe_2O_3 has been estimated, as shown in Table S3. It should be noted that because there were no Fe-related diffraction peaks in the XRD patterns for the $\text{Fe}_2\text{O}_3/\gamma\text{-Al}_2\text{O}_3$ samples with 1 wt.% and 3 wt.% loadings, the particle size and dispersion of these two samples are not available. Clearly, for other samples (5, 10, 20, and 25 wt.%), the average particle size gradually increased with the increasing of loadings.

Figure 3B shows the H_2 -TPR profiles of the $\text{Fe}_2\text{O}_3/\gamma\text{-Al}_2\text{O}_3$ samples with various loadings. At low loading (i.e., 1, 3, and 5 wt.%), the broad peaks are concentrated at 210°C–340°C, which is due to the reduction of small Fe_2O_3 particles, as well as the consumption of adsorbed oxygen on the $\text{Fe}_2\text{O}_3/\gamma\text{-Al}_2\text{O}_3$ surface, as reported in literature.⁴³ With increasing Fe loading (i.e., 10–25 wt.%), the reduction peaks of the TPR are concentrated around 340°C–470°C, which corresponds to the reduction of bigger Fe_2O_3 particles to Fe_3O_4 .^{44,45} The high-temperature reduction peaks between 470°C–780°C are attributed to the reduction of Fe_3O_4 to FeO and of FeO to Fe .

The crystal structure and morphology of the $\text{Fe}_2\text{O}_3/\gamma\text{-Al}_2\text{O}_3$ catalyst (5 wt.% loading) was further characterized by HRTEM. As shown in Figure 3C,D, Fe_2O_3 is uniformly dispersed on the support, and clear lattice fringes with a space of 0.252 and 0.270 nm, attributed to the (110) and (104) crystal plane of $\alpha\text{-Fe}_2\text{O}_3$, respectively, are observed.⁴⁶ Furthermore, the STEM image (Figure 3E) also shows highly dispersed Fe_2O_3 particles, which can be demonstrated by line scanning results (Figure 3F), since Fe signals have been synchronously observed with the positions of three particles on the scanning line. The EDX mapping results (Figure S8) also show high dispersion of Fe in the $\text{Fe}_2\text{O}_3/\gamma\text{-Al}_2\text{O}_3$ catalyst.

The specific surface area (S_{BET}), volume of pores (V_p), and average pore diameter of the $\text{Fe}_2\text{O}_3/\gamma\text{-Al}_2\text{O}_3$ samples with various loadings and Fe-based catalysts with different supports are shown in Table S4. After associating reaction performance with the specific surface area and pore structure, we did not find any relationships between catalytic performance and S_{BET} or V_p . This is in line with our previous work.^{47,48} It may be attributed to the fact that the reactive plasma species directly regulate the catalyst surface reactions mainly via the Eley–Rideal (E–R) mechanism, and reactive plasma species are not often present inside catalyst pores. Indeed, plasma formation can only occur inside catalyst pores when the pore diameter is larger than the Debye length (which is around 600 nm at typical plasma catalysis conditions^{49,50}). For smaller pores, plasma species could in principle still diffuse into the pore, but due to their high reactivity, they easily react with the pore surface, before reaching deeper inside the pore.

Figure 4A,B show the XPS spectra of Fe 2p and O 1s of $\text{Fe}_2\text{O}_3/\gamma\text{-Al}_2\text{O}_3$ catalysts with various Fe loading. In the range of 705–730 eV (Figure 4A), five peaks corresponding to the binding energy of 709.5, 710.5, 712.2, 718.7, and 724.5 eV were detected. They are attributed to $2p_{3/2}$ of Fe^{II} species, $2p_{3/2}$ of Fe^{III} octahedral species, $2p_{3/2}$ of Fe^{III}

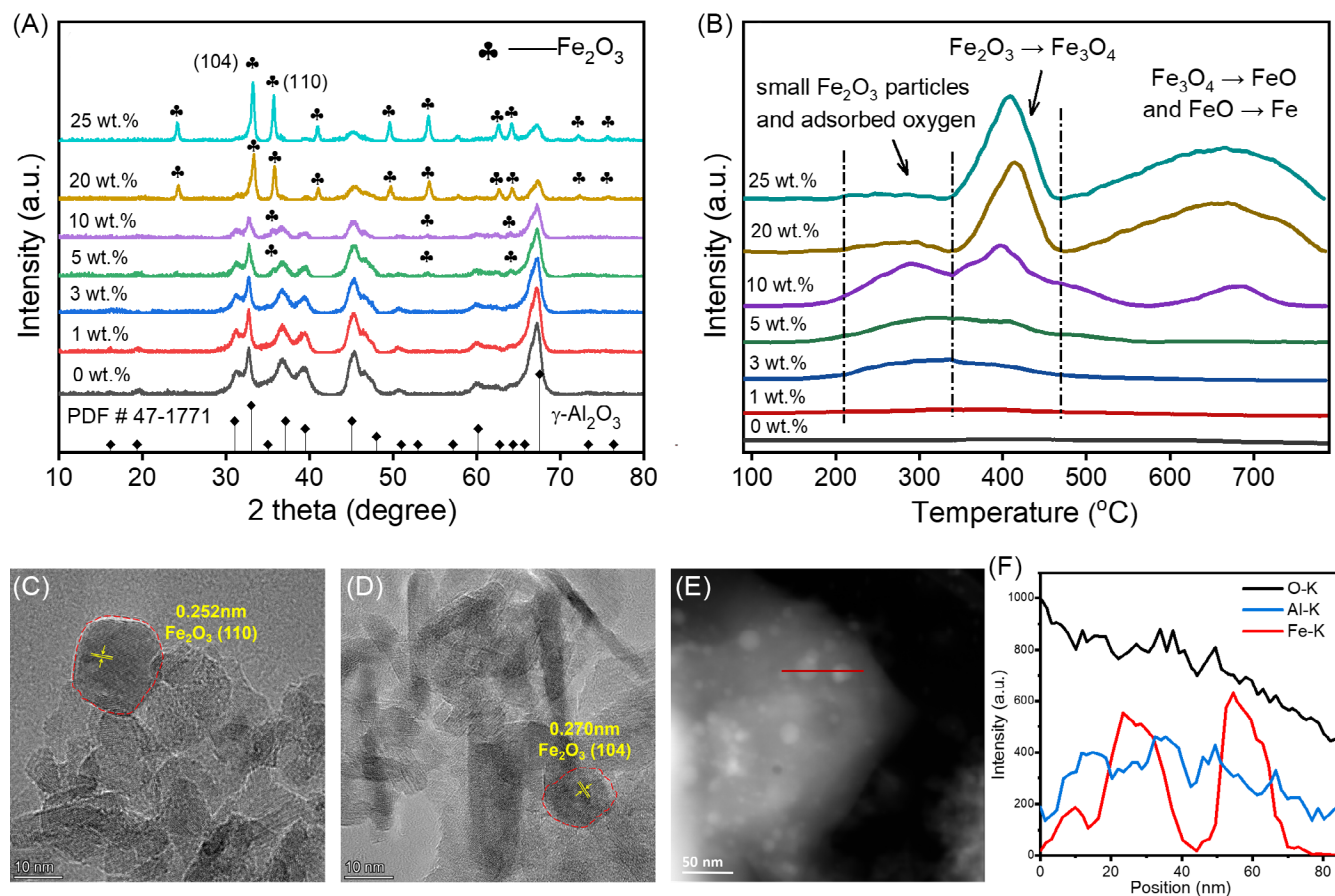


FIGURE 3 Characterization results of the fresh 5 wt.% $\text{Fe}_2\text{O}_3/\gamma\text{-Al}_2\text{O}_3$ catalysts. (A) x-ray powder diffraction (XRD) patterns; (B) hydrogen temperature programmed reduction (H_2 -TPR) profiles; (C,D) high-resolution transmission electron microscopy (HRTEM) results; (E) scanning transmission electron microscopy (STEM) results; (F) Energy spectrum of the STEM.

tetrahedral species, a satellite peak of Fe^{III} species ($2p_{3/2}$), and a satellite peak of $2p_{1/2}$ of Fe^{III} species, respectively.^{51,52} We can see that at low loadings (1 and 3 wt.%), only Fe^{III} species were observed. At higher loadings (5, 10, 20, and 25 wt.%), however, besides Fe^{III} species, some Fe^{II} species were detected on the surface of the $\text{Fe}_2\text{O}_3/\gamma\text{-Al}_2\text{O}_3$ catalyst. As shown in Figure 4B, the O 1s spectra of the $\text{Fe}_2\text{O}_3/\gamma\text{-Al}_2\text{O}_3$ catalysts can be fitted into two peaks corresponding to lattice oxygen (O_α) and chemisorbed oxygen (O_β) of the metal oxides, with binding energy of 530.8 and 532.1 eV, respectively.^{46,53}

As shown in Figure 4C, with increasing Fe loading from 1 to 5 wt.%, the proportion of O_β species on the catalyst surface rises, and reaches the highest value (24.8%) at 5 wt.% loading, and then it decreases. Combined with the XRD and H_2 -TPR results, we can conclude that the chemisorbed oxygen, that is, O_β species, mainly come from the interface between the highly dispersed Fe_xO_y particles and the $\gamma\text{-Al}_2\text{O}_3$ support. At low loadings (1 and 3 wt.%), the Fe content is very low, leading to a low interface surface area, which causes a small proportion of O_β species. At high loadings (10, 20, and 25 wt.%), the Fe content is enough, but the size of the Fe_xO_y particles is too big (Table S3), resulting in a low dispersion of Fe and again a low interface surface area, which causes a small proportion of O_β species as well. Therefore, the highest proportion of O_β species was detected at

moderate loading (5 wt.%). Lattice oxygen, that is, O_α species, are undoubtedly from the crystals, that is, the $\gamma\text{-Al}_2\text{O}_3$ support and the Fe_xO_y particles. Upon increasing Fe loading, the proportion of O_α species, however, first decreases and then increases, and the lowest proportion was found at 5 wt.% loading, which means that there are more defects on the surface of the 5 wt.% $\text{Fe}_2\text{O}_3/\gamma\text{-Al}_2\text{O}_3$ catalyst than on the other catalysts. It is clear that the defects are created at the interface between the highly dispersed Fe_xO_y particles and the $\gamma\text{-Al}_2\text{O}_3$ support. Briefly, the O_α species are undoubtedly from the crystal, that is, the $\gamma\text{-Al}_2\text{O}_3$ support and big/free Fe_2O_3 particles with weak oxide-support interaction (WOSI). The O_β species, however, mainly come from strong oxide-support interaction (SOSI) between Fe_2O_3 particles and $\gamma\text{-Al}_2\text{O}_3$ support.^{47,54}

Figure 4D presents the reaction performance (CO_2 conversion, CH_3OH , and CO selectivity) as a function of O_β content at the catalyst surface. Interestingly, with increasing O_β content, both CO_2 conversion and CH_3OH selectivity rise linearly, while the CO selectivity decreases linearly. Furthermore, the O_β content of $\text{CuO}/\gamma\text{-Al}_2\text{O}_3$ also applies to these linear rules (Figure S9). These results clearly suggest that, for CO_2 hydrogenation to CH_3OH in our study, chemisorbed oxygen, that is, O_β species, may be a key intermediate, and the defects resulting in O_β species at the interface between Fe_xO_y and $\gamma\text{-Al}_2\text{O}_3$

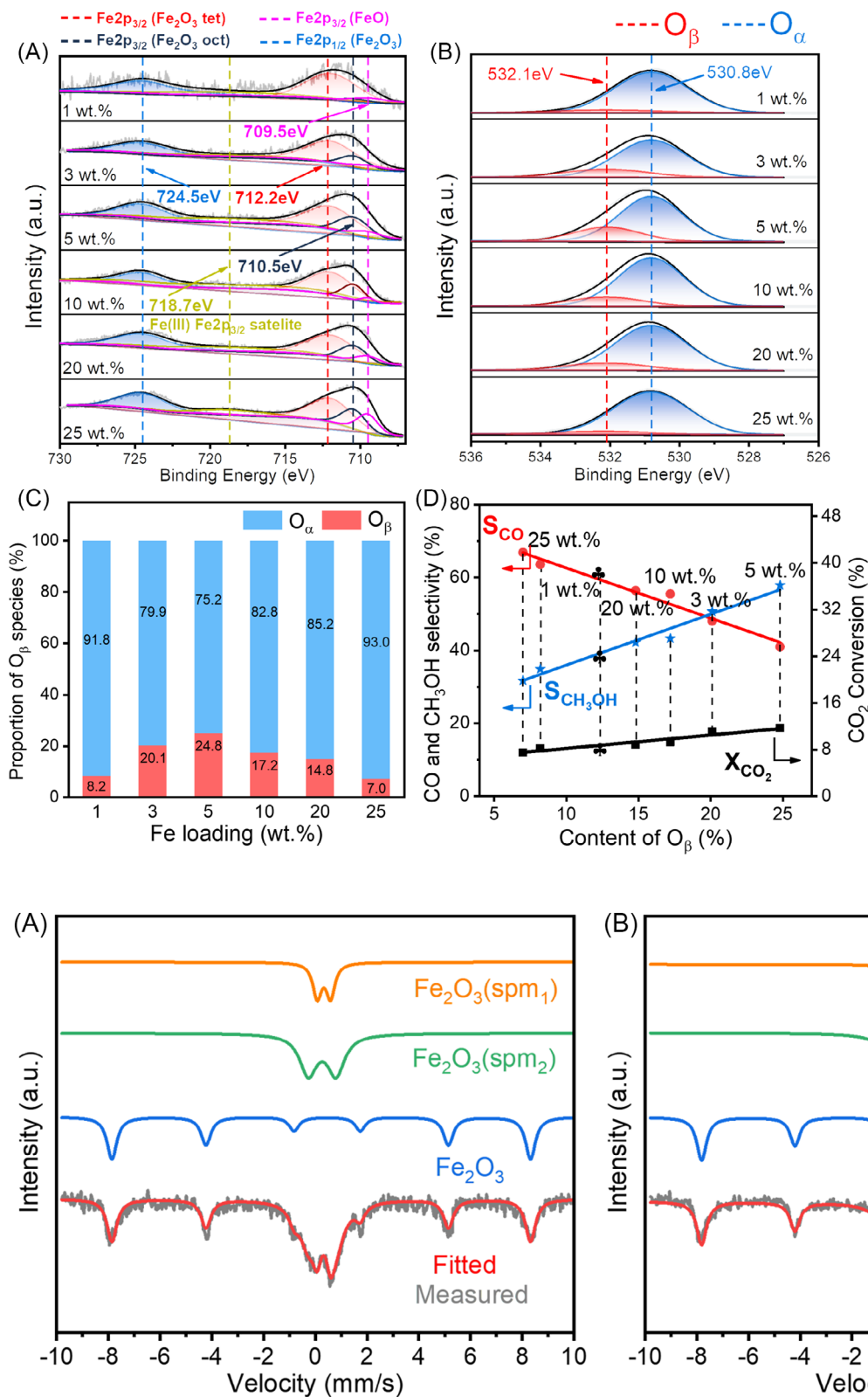


FIGURE 4 X-ray photoelectron spectroscopy (XPS) spectra of the $Fe_2O_3/\gamma-Al_2O_3$ catalyst at various loadings. (A) Fe 2p region; (B) O 1s region; (C) Proportion of lattice oxygen (O_{α}) and chemisorbed oxygen (O_{β}) species; (D) Relationship between O_{β} content and reaction performance (i.e., CO_2 conversion, CH_3OH and CO selectivity, ● represents CO selectivity, ★ represents CH_3OH selectivity, ■ represents CO_2 conversion, ♣ represents $CuO/\gamma-Al_2O_3$ catalyst with 5 wt.% loading). The standard charge was calibrated by C 1s binding energy of 284.8 eV.

FIGURE 5 Mössbauer spectra of (A) fresh and (B) spent 5 wt.% $Fe_2O_3/\gamma-Al_2O_3$ catalysts.

may be the real active sites. The reason why 5 wt.% $Fe_2O_3/\gamma-Al_2O_3$ catalyst has the best catalytic performance is that it possesses the most abundant O_{β} species. Therefore, a plausible mechanism of

chemisorbed oxygen species or defects on the catalyst surface to catalyze CO_2 hydrogenation has been proposed in the section of Reaction Mechanism.

The spent catalysts have been characterized by XRD, ^{57}Fe Mössbauer spectroscopy, H_2 -TPR, XPS, and HRTEM. The XRD patterns of the spent catalysts (Figure S10) were almost identical to those of the fresh catalysts (Figure 3A), which means that the bulk phase of $\text{Fe}_2\text{O}_3/\gamma\text{-Al}_2\text{O}_3$ catalyst did not change significantly during CO_2/H_2 plasma reaction. The fresh and spent 5 wt.% $\text{Fe}_2\text{O}_3/\gamma\text{-Al}_2\text{O}_3$ catalysts were characterized by the ^{57}Fe Mössbauer spectroscopy (Figure 5 and Table S5). The results show that all Fe species in the catalyst are present as Fe_2O_3 , and no Fe carbide phases were found after the reaction.⁵⁵ The six-element peak is the typical structure of Fe_2O_3 , while the symmetrical double peaks are super-paramagnetic Fe_2O_3 in different environments, indicating two kinds of distortion degrees in their environment surrounding.⁵⁶

Figure S11a shows the H_2 -TPR profiles of the spent $\text{Fe}_2\text{O}_3/\gamma\text{-Al}_2\text{O}_3$ catalyst with varied loadings. Figure S11b shows the H_2 -TPR profiles of fresh and spent $\text{Fe}_2\text{O}_3/\gamma\text{-Al}_2\text{O}_3$ catalyst with 5 wt.% loading. Clearly, the intensity of H_2 consumption peak of the spent sample is a little lower than that of the fresh sample (Figure S11b), which demonstrates that the $\text{Fe}_2\text{O}_3/\gamma\text{-Al}_2\text{O}_3$ catalyst has been partially reduced by CO_2/H_2 plasma. The XPS spectra of the fresh and spent $\text{Fe}_2\text{O}_3/\gamma\text{-Al}_2\text{O}_3$ catalyst (5 wt.% loading) are shown in Figure S12. It can be seen that, compared with the fresh sample, the spent sample shows a slightly higher peak of Fe^{II} species in the spectra of Fe 2p (Figure S12a), which means that the surface Fe^{III} species has been partially reduced to Fe^{II} species by CO_2/H_2 plasma. Accordingly, the intensity of O 1s spectra of the spent sample is a slightly lower than that of the fresh sample (Figure S12b), also indicating a partial reduction of $\text{Fe}_2\text{O}_3/\gamma\text{-Al}_2\text{O}_3$ catalyst. However, peak fitting results (Figure S12c) indicate that the content of O_β increased from 23.5% (fresh sample) to 25.7% (spent sample), which may be caused by interaction of air with the high reactive defects ($\text{Fe}_2\text{O}_3/\gamma\text{-Al}_2\text{O}_3$ interface) created by CO_2/H_2 plasma through modification during the reaction process. Therefore, the gradually increased CO_2 conversion and CH_3OH selectivity during the 60 h continuous operation (Figure 2D) could be attributed to the modification of $\text{Fe}_2\text{O}_3/\gamma\text{-Al}_2\text{O}_3$ catalyst by CO_2/H_2 plasma, which partially reduced Fe^{III} to Fe^{II} species, creating more defects at $\text{Fe}_2\text{O}_3/\gamma\text{-Al}_2\text{O}_3$ interface to generate more O_β species and promote CO_2 activation and subsequent hydrogenation reaction. Although Fe carbide phases can be formed on Fe oxide surfaces during conventional thermal catalytic CO_2 hydrogenation reaction, we did not observe any Fe carbide phases over the spent $\text{Fe}_2\text{O}_3/\gamma\text{-Al}_2\text{O}_3$ catalyst by XRD (Figure S10), Mössbauer spectroscopy (Figure 5), XPS (Figure S12) or HRTEM (Figure S13), which may be caused by different reaction temperature and pressure between thermal catalysis and plasma catalysis.^{57,58}

We also compared the catalytic performances of both metallic and metal oxide state of iron on $\gamma\text{-Al}_2\text{O}_3$ (Figure S14a). The CO_2 conversion and CO selectivity gradually decreased within 45 min and then remained stable. However, CH_3OH selectivity gradually increased and then remained stable. These experimental results demonstrate that the fresh metallic $\text{Fe}/\gamma\text{-Al}_2\text{O}_3$ catalyst does not favor generation of CH_3OH , but promote production of CO through RWGS reaction. The corresponding spent catalyst has been characterized by H_2 -TPR (Figure S14b), and an obvious H_2 consumption peak has been

observed. That is, the fresh metallic $\text{Fe}/\gamma\text{-Al}_2\text{O}_3$ catalyst cannot remain the Fe^0 valence state during the CO_2/H_2 plasma reaction, and it has been partially oxidized, which may be caused by oxidation function of O atoms from CO_2 dissociation during plasma-catalytic CO_2 hydrogenation reaction. On the other hand, characterization results of the spent $\text{Fe}_2\text{O}_3/\gamma\text{-Al}_2\text{O}_3$ catalyst (Figures S11 and S12) indicate a partially reduction process, which may be caused by H species from H_2 dissociation since it played a role of reducing agent. Therefore, the CO_2/H_2 plasma reaction catalyzed by $\text{Fe}_2\text{O}_3/\gamma\text{-Al}_2\text{O}_3$ catalyst contains a dynamic reduction-oxidation process, yielding a dynamic reduction-oxidation of the Fe species.

3.3 | Adsorption properties of different supports

Figure S5 shows that $\gamma\text{-Al}_2\text{O}_3$ is the optimized support of iron-based catalysts for plasma-catalytic CO_2 hydrogenation to produce CH_3OH . To understand the support effects, we investigated the adsorption properties of different supports through diffuse reflectance infrared Fourier transform spectroscopy (DRIFTs), as shown in Figure 6A,B. The peaks appearing at 2347 and 667 cm^{-1} in the spectra are attributed to the asymmetric stretching vibration mode and deformation vibration mode of adsorbed CO_2 , respectively.⁵⁹ The broad peak near 1657 cm^{-1} is assigned to carbonate (CO_3^{2-}).⁶⁰ Specifically, comparing the DRIFTs of the samples after CO_2 adsorption and subsequent CO_2 desorption, we can conclude that TiO_2 , SiO_2 and In_2O_3 have relatively weak adsorption capacity for CO_2 , since the peaks of CO_2 nearly disappear after 10 minutes desorption. For the other supports, that is, CeO_2 , ZrO_2 , $\text{Al}(\text{OH})_3$ and $\gamma\text{-Al}_2\text{O}_3$, the peaks of CO_2 still exist after 10 minutes desorption, indicating that these support materials have relatively stronger adsorption capacity for CO_2 . Furthermore, the CO_2 adsorption capacity of the Fe-based catalysts with different supports has been investigated by temperature program desorption (TPD) technique, and the CO_2 -TPD profiles are shown in Figure 6C. Clearly, $\text{Fe}_2\text{O}_3/\text{CeO}_2$, $\text{Fe}_2\text{O}_3/\text{ZrO}_2$, $\text{Fe}_2\text{O}_3/\text{Al}(\text{OH})_3$ and $\text{Fe}_2\text{O}_3/\gamma\text{-Al}_2\text{O}_3$ catalysts show relative higher peaks of CO_2 desorption, which further indicates that these catalysts have relatively stronger adsorption capacity for CO_2 . Correspondingly, they show a strong plasma-catalytic CO_2 hydrogenation, but the $\text{Fe}_2\text{O}_3/\gamma\text{-Al}_2\text{O}_3$ catalyst has the highest CO_2 conversion and CH_3OH selectivity (Figure S5b,d).

Since CO is the most abundant by-product in this plasma catalytic CO_2 hydrogenation, we also studied the adsorption capacity of Fe-based catalysts for CO by TPD, and the CO-TPD profiles are shown in Figure 6D. It can be seen that $\text{Fe}_2\text{O}_3/\gamma\text{-Al}_2\text{O}_3$ and $\text{Fe}_2\text{O}_3/\text{Al}(\text{OH})_3$ catalysts exhibit much higher CO desorption peaks than other catalysts, and the dominant desorption temperature is above 400 °C. These results demonstrate that $\text{Fe}_2\text{O}_3/\gamma\text{-Al}_2\text{O}_3$ and $\text{Fe}_2\text{O}_3/\text{Al}(\text{OH})_3$ can strongly adsorb CO molecule with relative high adsorbing capacity, leading to hydrogenation of CO into CH_xO species, and further hydrogenation reaction to produce CH_3OH through RWGS pathway, which may be the main reason why $\text{Fe}_2\text{O}_3/\gamma\text{-Al}_2\text{O}_3$ and $\text{Fe}_2\text{O}_3/\text{Al}(\text{OH})_3$

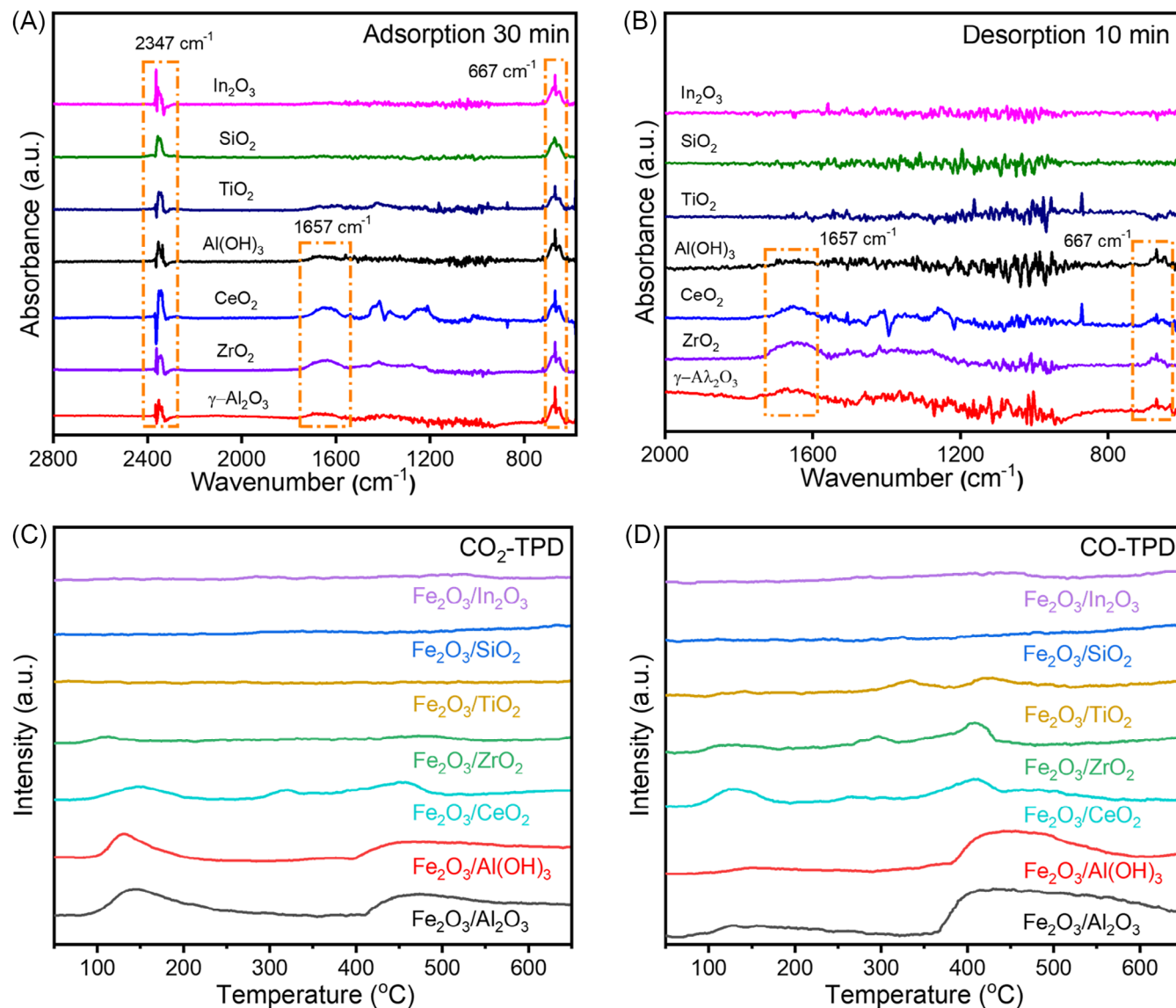


FIGURE 6 CO₂-diffuse reflectance infrared Fourier transform spectroscopy (DRIFT) spectra of different supports: (A) Adsorption: 30 min; (B) Desorption: 10 min; (C,D) the adsorption capacity of Fe-based catalysts: (C) CO₂ and CO temperature programmed desorption (CO₂-TPD) and (D) CO-TPD.

exhibit relative high CH₃OH selectivity but low CO selectivity (Figure S5b,d).

3.4 | Plasma diagnostics

In-situ OES diagnostics were carried out to analyze the species in the H₂/CO₂ plasma (Figure 7). DBD plasma is capable of activating H₂ and CO₂ to produce a variety of chemically reactive species, including radicals, excited atoms and molecules, and ions. As shown in Figure 7A, we observed several spectral lines and bands, including the H_α line (656.3 nm, 3d²D → 2p²P⁰), the CO Angstrom band (451–608 nm, B¹Σ → A¹Π) and two O atom lines (777.5 nm, 3s⁵S⁰ → 3p⁵P; and 844.7 nm, 3s³S⁰ → 3p³P), from the H₂/CO₂ plasma.²⁴ However, the signal intensities are different in plasma only

vs plasma with γ-Al₂O₃ support and with Fe₂O₃/γ-Al₂O₃ catalyst. Indeed, compared with the pure H₂/CO₂ plasma, the signal intensity becomes weaker after packing with the γ-Al₂O₃ support, attributed to shielding by the packing.⁶¹ In the case of packing with Fe₂O₃/γ-Al₂O₃, the signal intensity is further reduced. It can be seen from Figure S15 that the Fe₂O₃/γ-Al₂O₃ catalyst shows obvious absorption peaks for both UV-light (200–400 nm) and visible light (400–800 nm). Hence, the reduction of OES intensity is not only attributed to optical interference from the packed catalysts, but the active sites also play an important role in the absorption of the plasma-active species. Specifically, Figure 7B shows the spectral signal of CO in the three different cases. The H₂/CO₂ plasma packed by Fe₂O₃/γ-Al₂O₃ clearly shows the lowest signal intensity, caused by strong adsorption of CO at the catalyst (indicated as CO*). The adsorbed CO* may lead to CH₃OH production through hydrogenation reactions with adsorbed

FIGURE 7 In-situ optical emission spectra of H_2/CO_2 DBD plasma: (a) Full wavelength OES; (b) Partial wavelength OES. (1 s exposure time).

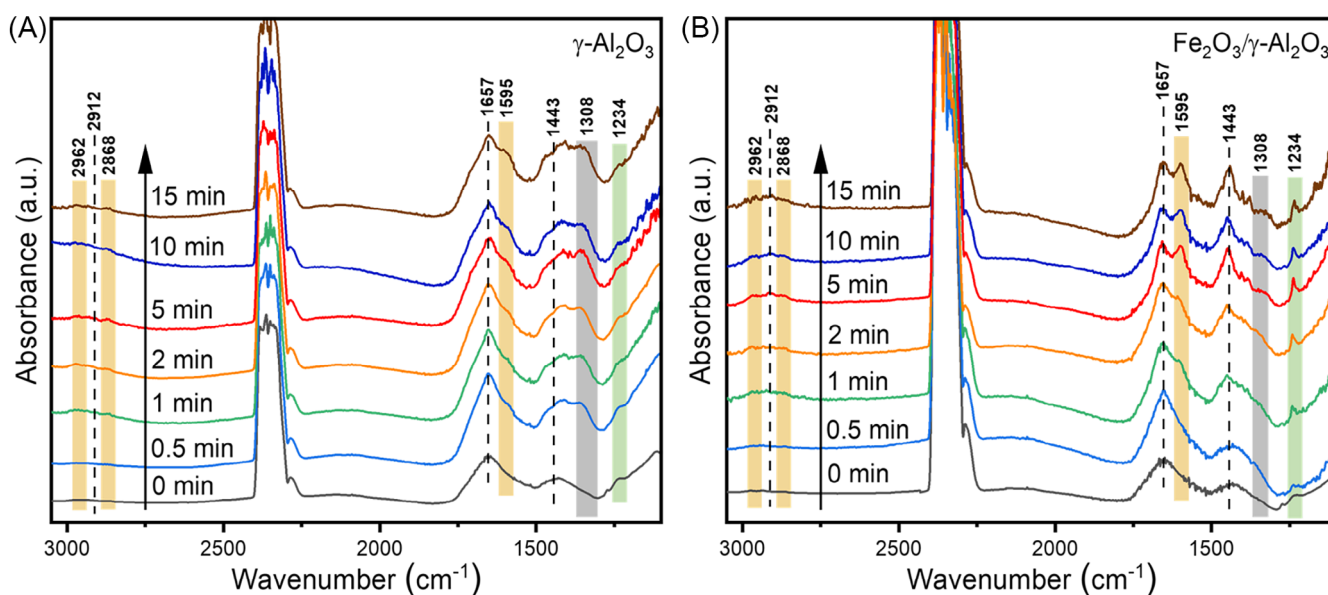
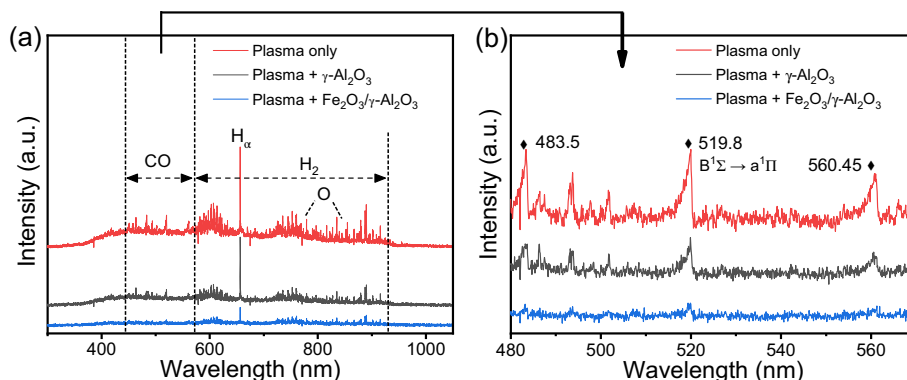


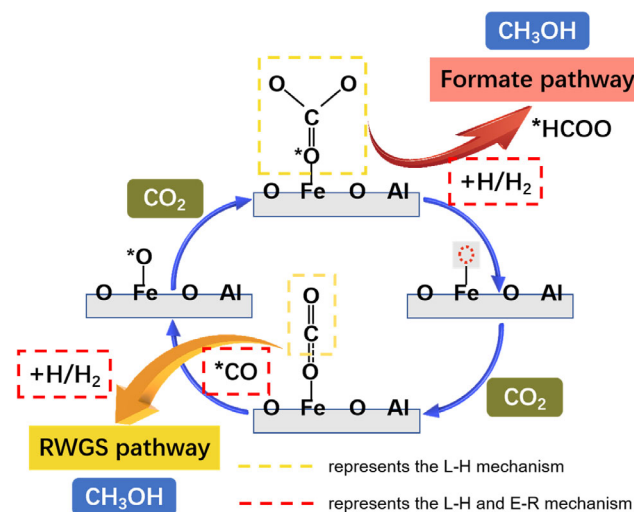
FIGURE 8 *In situ* diffuse reflectance infrared Fourier transform spectroscopy (DRIFTS) spectra of surface species on the (A) $\gamma\text{-Al}_2\text{O}_3$ support and (B) $\text{Fe}_2\text{O}_3/\gamma\text{-Al}_2\text{O}_3$ catalyst. (discharge voltage 24 kV, discharge frequency 9.5 kHz, discharge power 14.4 W, $\text{CO}_2/\text{H}_2 = 1/3$, flow rate = 40 mL/min).

$\text{H}(\text{s})$ and plasma-phase $\text{H}(\text{g})$ species, as predicted by DFT calculations.^{24,48} This is in line with our observations that the highest CO selectivity and the lowest CH_3OH selectivity were obtained in the case of only H_2/CO_2 plasma, while the lowest CO selectivity and the highest CH_3OH selectivity were reached in the case of plasma with $\text{Fe}_2\text{O}_3/\gamma\text{-Al}_2\text{O}_3$ packing. The reactive CO and H species can promote the CH_3OH production via E-R reactions over the catalyst surface, and the possible E-R reactions are shown in Table S6.

3.5 | Reaction mechanism

To elucidate the reaction mechanism of plasma-catalytic CO_2 hydrogenation to CH_3OH over $\text{Fe}_2\text{O}_3/\gamma\text{-Al}_2\text{O}_3$ catalyst, the active intermediates on $\gamma\text{-Al}_2\text{O}_3$ support and $\text{Fe}_2\text{O}_3/\gamma\text{-Al}_2\text{O}_3$ catalyst were examined using an *in situ* DRIFTS setup (Figure S16). As shown in Figure 8, the peaks related to CO_2 molecule can be easily seen at

2347 cm^{-1} . The peak intensity of surface carbonates at 1595 cm^{-1} and 1657 cm^{-1} gradually increases after plasma on, implying the presence of carbonate species is not only due to physical adsorption of CO_2 , but also attributed to plasma excitation, that is, vibrational excitation of CO_2 adsorbed on the catalyst surface.⁶² The bicarbonate species (b-HCO_3^*) at 1234 cm^{-1} were also observed (green rectangular shading), and it was converted into the formate species (HCOO^*) on the surface of the $\text{Fe}_2\text{O}_3/\gamma\text{-Al}_2\text{O}_3$ catalyst (ca. 1595, 2868, and 2962 cm^{-1} , yellow rectangular shading) as the reaction proceeded.⁶³ The presence of the CH_3O^* species at 2912 cm^{-1} represents the formation of CH_3OH ($\text{V}_{\text{as}}\text{CH}_3$),⁶⁴ indicating that the formate species on the catalyst surface may be a key intermediate for methanol synthesis. The peak at 1308 cm^{-1} is attributed to the formyl species (CH_xO^*), and the formation of CH_xO^* species under plasma conditions may be attributed to a large number of CO and H species, which can be confirmed by OES results (Figure 7).^{62,65} By comparing the peak intensity related to HCOO^* , CH_3O^* and HCO_3^* species, $\text{Fe}_2\text{O}_3/\gamma\text{-Al}_2\text{O}_3$



SCHEME 1 Possible reaction mechanism of CO₂ hydrogenation to CH₃OH over Fe₂O₃/γ-Al₂O₃ catalyst driven by plasma. Highlighting the role of (O_p) species in promoting CO₂ hydrogenation through formate pathway and subsequent CO₂ hydrogenation through RWGS pathway after CH₃OH desorption. (Yellow frame represents L-H mechanisms, and red frame represents L-H and E-R mechanisms)

catalyst obviously shows a much higher intensity than γ-Al₂O₃ support, which further demonstrate the catalytic role of Fe species on γ-Al₂O₃ in promoting CO₂/H₂ plasma reaction to produced CH₃OH.⁶⁶ It should be noted that the linearly adsorbed CO_{ad} was not detected in Figure 8. However, at a relative higher input power (Figure S17), the peaks at 2170 and 2115 cm⁻¹ reveal linear adsorption of CO on the catalyst surface, which further proves that higher discharge power favors RWGS reaction to produce CO.

Based on above-mentioned discussion, a possible reaction mechanism of CO₂ hydrogenation to CH₃OH over Fe₂O₃/γ-Al₂O₃ catalyst has been proposed, as shown in Scheme 1. Firstly, the chemisorbed oxygen species tends to adsorb CO₂ molecule (Figure 6A,B), forming adsorbed CO₃* species (at 1443 and 1657 cm⁻¹ in DRIFTS spectra), which in the presence of H₂, can be hydrogenated into HCOO* species (at 1595, 2868, and 2962 cm⁻¹ in DRIFTS spectra).^{60,67} This species is the key intermediate for CO₂ hydrogenation to CH₃OH through the formate pathway. Then, after desorption of CH₃OH molecule, produced by the formate pathway, a vacancy of the adsorbed oxygen is generated at the interface of Fe₂O₃/γ-Al₂O₃, which corresponds to the partially reduction of Fe^{III} to Fe^{II} species (Figures S11b and S12a). While, the vacancy of adsorbed oxygen is capable of interacting with the O atom of CO₂ molecule, which can activate CO₂ molecule and dissociate C=O bond in the presence of H₂ (at 2115 and 2170 cm⁻¹ in DRIFTS spectra). After that, the produced CO can be strongly adsorbed over Fe₂O₃/γ-Al₂O₃ catalyst (Figure 6D), and subsequent hydrogenation through RWGS reaction pathways leads to CH₃OH formation. In one word, the chemisorbed oxygen species can be considered as an intermediate in this plasma catalytic CO₂ hydrogenation to CH₃OH over the Fe₂O₃/γ-Al₂O₃ catalyst.

4 | CONCLUSION

In summary, we investigated several catalysts for CO₂ hydrogenation into CH₃OH by plasma catalysis, and showed the best performance for Fe₂O₃/γ-Al₂O₃ catalyst, demonstrating a clear synergy of the CO₂/H₂ plasma with the Fe₂O₃/γ-Al₂O₃ catalyst, at a temperature of nearly 80°C and atmospheric pressure. At optimized reaction conditions (residence time, CO₂/H₂ mole ratio, discharge power, and circulating water temperature) and optimized Fe-based catalysts (support and Fe loading), we achieved 12% CO₂ conversion with 58% CH₃OH selectivity, and an energy consumption of 19.8 kJ/mmol, which is almost 9 times lower than in case of plasma alone (181.7 kJ/mmol). XPS characterization of the catalysts shows that both CO₂ conversion and CH₃OH selectivity rise linearly with the fraction of chemisorbed oxygen species at the Fe₂O₃/γ-Al₂O₃ catalyst, which strongly suggests that the chemisorbed oxygen species are the key intermediate, and the defects resulting in O_p species at the Fe₂O₃/γ-Al₂O₃ interface are the real active sites, for CO₂ hydrogenation to CH₃OH in our study. Furthermore, our CO₂-DRIFTS, CO₂-TPD, and CO-TPD results show that catalysts with stronger adsorption capacity of CO₂ exhibit a higher CO₂ conversion and CH₃OH selectivity. *In situ* DRIFTS results reveal that Fe species on γ-Al₂O₃ provides more active sites to form surface reaction intermediates, that is, HCOO*, CH₃O*, and HCO₃* species, which enhance CH₃OH synthesis from CO₂/H₂ plasma reaction. As mentioned above, of all the metals we investigated, Fe performed clearly the best. Therefore, our paper is very useful to expand the number of catalytic systems and to design highly efficient catalysts, for plasma-catalytic CO₂ hydrogenation into CH₃OH at ambient condition.

AUTHOR CONTRIBUTIONS

Shengyan Meng: Conceptualization (equal); data curation (equal); formal analysis (equal); resources (equal); validation (equal); writing – original draft (equal); writing – review and editing (equal). **Liang Wu:** Data curation (equal); formal analysis (equal); resources (equal). **Miao Liu:** Conceptualization (equal); data curation (equal); formal analysis (equal); resources (equal); validation (equal). **Zhaolun Cui:** Data curation (equal); formal analysis (equal); validation (equal). **Qian Chen:** Data curation (equal); resources (equal). **Shangkun Li:** Data curation (equal); formal analysis (equal); resources (equal); validation (equal). **Jiahui Yan:** Formal analysis (equal); validation (equal). **Li Wang:** Formal analysis (equal); validation (equal). **Xinkui Wang:** Data curation (equal); resources (equal). **Ji Qian:** Data curation (equal); resources (equal). **Hongchen Guo:** Data curation (equal); resources (equal). **Jinhai Niu:** Conceptualization (equal); data curation (equal); formal analysis (equal); resources (equal); supervision (equal); validation (equal). **Annemie Bogaerts:** Data curation (equal); formal analysis (equal); funding acquisition (equal); resources (equal); supervision (equal); writing – original draft (equal); writing – review and editing (equal). **Yanhui Yi:** Conceptualization (equal); data curation (equal); formal analysis (equal); funding acquisition (equal); resources (equal); supervision (equal); validation (equal); writing – original draft (equal); writing – review and editing (equal).

ACKNOWLEDGMENTS

We acknowledge financial support from the National Natural Science Foundation of China [21978032, 21908016] and the Fundamental Research Funds for the Central Universities of China [DUT18JC42].

DATA AVAILABILITY STATEMENT

The data that support the findings of this study are available from the corresponding author upon reasonable request.

ORCID

Yanhui Yi  <https://orcid.org/0000-0002-5869-9382>

REFERENCES

- Zhong JW, Yang XF, Wu ZL, Liang BL, Huang YQ, Zhang T. State of the art and perspectives in heterogeneous catalysis of CO₂ hydrogenation to methanol. *Chem Soc Rev.* 2020;49(5):1385-1413.
- Bui M, Adjiman CS, Bardow A, et al. Carbon capture and storage (CCS): the way forward. *Energ Environ Sci.* 2018;11(5):1062-1176.
- Von der Assen N, Voll P, Peters M, Bardow A. Life cycle assessment of CO₂ capture and utilization: a tutorial review. *Chem Soc Rev.* 2014;43(23):7982-7994.
- Arena F, Barbera K, Italiano G, Bonura G, Spadaro L, Frusteri F. Synthesis, characterization and activity pattern of Cu-ZnO/ZrO₂ catalysts in the hydrogenation of carbon dioxide to methanol. *J Catal.* 2007;249(2):185-194.
- Chen SY, Zhang JF, Song FE, et al. Induced high selectivity methanol formation during CO₂ hydrogenation over a CuBr₂-modified CuZnZr catalyst. *J Catal.* 2020;389:47-59.
- Shen CY, Sun KH, Zou R, Wu QL, Mei DH, Liu CJ. CO₂ hydrogenation to methanol on indium oxide-supported rhenium catalysts: the effects of size. *ACS Catal.* 2022;12(20):12658-12669.
- Rui N, Zhang F, Sun KH, et al. Hydrogenation of CO₂ to methanol on a Au^{δ+}-In₂O_{3-x} catalyst. *ACS Catal.* 2020;10(19):11307-11317.
- Yao LB, Shen XC, Pan YB, Peng ZM. Synergy between active sites of Cu-In-Zr-O catalyst in CO₂ hydrogenation to methanol. *J Catal.* 2019;372:74-85.
- Xu SJ, Chansai S, Stere C, et al. Sustaining metal-organic frameworks for water-gas shift catalysis by non-thermal plasma. *Nat. Catal.* 2019;2(2):142-148.
- Snoeckx R, Bogaerts A. Plasma technology-a novel solution for CO₂ conversion? *Chem Soc Rev.* 2017;46(19):5805-5863.
- Mehta P, Barboun P, Herrera FA, et al. Overcoming ammonia synthesis scaling relations with plasma-enabled catalysis. *Nat Catal.* 2018;1(4):269-275.
- Zhang X, Liu Y, Zhang MT, et al. Synergy between β-Mo₂C nanorods and non-thermal plasma for selective CO₂ reduction to CO. *Chem.* 2020;6(12):3312-3328.
- Zhang K, Harvey AP. CO₂ decomposition to CO in the presence of up to 50% O₂ using a non-thermal plasma at atmospheric temperature and pressure. *Chem Eng J.* 2021;405:126625.
- Zeng YX, Tu X. Plasma-catalytic CO₂ hydrogenation at low temperatures. *IEEE Transact Plasma Sci.* 2015;44(4):405-411.
- Zhu XB, Liu JH, Li XS, Liu JL, Qu X, Zhu AM. Enhanced effect of plasma on catalytic reduction of CO₂ to CO with hydrogen over Au/-CeO₂ at low temperature. *J Energy Chem.* 2017;26(3):488-493.
- Xu SS, Chansai S, Shao Y, et al. Mechanistic study of non-thermal plasma assisted CO₂ hydrogenation over Ru supported on MgAl layered double hydroxide. *Appl Catal Environ.* 2020;268:118752.
- Biset-Peiró M, Guilera J, Zhang T, Arbiol J, Andreu T. On the role of ceria in Ni-Al₂O₃ catalyst for CO₂ plasma methanation. *Appl Catal Gen.* 2019;575:223-229.
- Biset-Peiró M, Mey R, Guilera J, Andreu T. Adiabatic plasma-catalytic reactor configuration: energy efficiency enhancement by plasma and thermal synergies on CO₂ methanation. *Chem Eng J.* 2020;393:124786.
- Da Costa P, Hasrack G, Bonnetty J, Henriques C. Ni-based catalysts for plasma-assisted CO₂ methanation. *Curr Opin Green and Sustain Chem.* 2021;32:100540.
- Chen HH, Mu YB, Shao Y, et al. Coupling non-thermal plasma with Ni catalysts supported on BETA zeolite for catalytic CO₂ methanation. *Cat Sci Technol.* 2019;9(15):4135-4145.
- Chen HH, Mu YB, Shao Y, et al. Nonthermal plasma (NTP) activated metal-organic frameworks (MOFs) catalyst for catalytic CO₂ hydrogenation. *AIChE J.* 2020;66(4):e16853.
- Joshi N, Sivachandiran L. Exploring the feasibility of liquid fuel synthesis from CO₂ under cold plasma discharge: role of plasma discharge in binary metal oxide surface modification. *RSC Adv.* 2021;11(44):27757-27766.
- Wang L, Yi YH, Guo HC, Tu X. Atmospheric pressure and room temperature synthesis of methanol through plasma-catalytic hydrogenation of CO₂. *ACS Catal.* 2018;8(1):90-100.
- Cui ZL, Meng SY, Yi YH, et al. Plasma-catalytic methanol synthesis from CO₂ hydrogenation over supported Cu cluster catalyst: insights into the reaction mechanism. *ACS Catal.* 2022;12(2):1326-1337.
- Wang JY, Zhang GH, Zhu J, et al. CO₂ hydrogenation to methanol over In₂O₃-based catalysts: from mechanism to catalyst development. *ACS Catal.* 2021;11(3):1406-1423.
- Sun KH, Fan ZG, Ye JY, et al. Hydrogenation of CO₂ to methanol over In₂O₃ catalyst. *J CO₂ Util.* 2015;12:1-6.
- Len T, Bahri M, Ersen O, et al. Ultradispersed Mo/TiO₂ catalysts for CO₂ hydrogenation to methanol. *Green Chem.* 2021;23(18):7259-7268.
- Zhang ZT, Shen CY, Sun KH, Jia XY, Ye JY, Liu CJ. Advances in studies of the structural effects of supported Ni catalysts for CO₂ hydrogenation: from nanoparticle to single atom catalyst. *J Mater Chem A.* 2022;10:5792-5812.
- Niu JT, Liu HY, Jin Y, Fan BG, Qi WJ, Ran JY. Comprehensive review of Cu-based CO₂ hydrogenation to CH₃OH: insights from experimental work and theoretical analysis. *Int J Hydrogen Energy.* 2022;47:9183-9200.
- Sha F, Han Z, Tang S, Wang JJ, Li C. Hydrogenation of carbon dioxide to methanol over non-Cu-based heterogeneous catalysts. *ChemSusChem.* 2020;13(23):6160-6181.
- Albrecht M, Rodemerck U, Schneider M, Broering M, Baabe D, Kondratenko EV. Unexpectedly efficient CO₂ hydrogenation to higher hydrocarbons over non-doped Fe₂O₃. *Appl Catal Environ.* 2017;204:119-126.
- Xu D, Wang YQ, Ding MY, Hong XL, Liu GL, Tsang SCE. Advances in higher alcohol synthesis from CO₂ hydrogenation. *Chem.* 2021;7(4):849-881.
- Wang JJ, You ZY, Zhang QH, Deng WP, Wang Y. Synthesis of lower olefins by hydrogenation of carbon dioxide over supported iron catalysts. *Catal Today.* 2013;215:186-193.
- Yang B, Yu X, Halder A, et al. Dynamic interplay between copper tetramers and iron oxide boosting CO₂ conversion to methanol and hydrocarbons under mild conditions. *ACS Sustain Chem Eng.* 2019;7(17):14435-14442.
- Joshi N, Loganathan S. Methanol synthesis from CO₂ using Ni and Cu supported Fe catalytic system: understanding the role of nonthermal plasma surface discharge. *Plasma Processes Polym.* 2021;18(5):2000104.
- Zhang XB, Li Z, Guo QH, Zheng HY, Xie KC. Selective synthesis of mixed alcohols from syngas over catalyst Fe₂O₃/Al₂O₃ in slurry reactor. *Fuel Process Technol.* 2010;91(4):379-382.

37. Zhang H, Li L, Li XD, Wang WZ, Yan JH, Tu X. Warm plasma activation of CO₂ in a rotating gliding arc discharge reactor. *J CO₂ Util.* 2018;27:472-479.
38. Yi YH, Xu C, Wang L, et al. Selectivity control of H₂/O₂ plasma reaction for direct synthesis of high purity H₂O₂ with desired concentration. *Chem Eng J.* 2017;313:37-46.
39. Qiao JL, Liu YY, Hong F, Zhang JJ. A review of catalysts for the electroreduction of carbon dioxide to produce low-carbon fuels. *Chem Soc Rev.* 2014;43(2):631-675.
40. Wang GX, Chen JX, Ding YC, et al. Electrocatalysis for CO₂ conversion: from fundamentals to value-added products. *Chem Soc Rev.* 2021;50(8):4993-5061.
41. Das S, Pérez-Ramírez J, Ji G, et al. Core-shell structured catalysts for thermocatalytic, photocatalytic, and electrocatalytic conversion of CO₂. *Chem Soc Rev.* 2020;49(10):2937-3004.
42. Yb X, Jia XL, Liu XH. Supported Fe/MnO_x catalyst with Ag doping for remarkably enhanced catalytic activity in Fischer-Tropsch synthesis. *Cat Sci Technol.* 2018;8(7):1953-1970.
43. Cheng XM, Li KZ, Wei YG, Zhu X, Tian D. Modification of KNO₃ on the reducibility and reactivity of Fe₂O₃-based oxygen carriers for chemical-looping combustion of methane. *Can J Chem Eng.* 2017; 95(8):1569-1578.
44. Oliveira LCA, Rios R, Fabris JD, Garg V, Sapag K, Lago RM. Activated carbon/iron oxide magnetic composites for the adsorption of contaminants in water. *Carbon.* 2002;40(12):2177-2183.
45. Zhou H, Li KK, Zhao BT, Deng WY, Su YX, Zhong FC. Surface properties and reactivity of Fe/Al₂O₃/cordierite catalysts for NO reduction by C₂H₆: effects of calcination temperature. *Chem Eng J.* 2017;326: 737-744.
46. Ouyang J, Zhao Z, Suib SL, Yang HM. Degradation of Congo red dye by a Fe₂O₃@CeO₂-ZrO₂/Palygorskite composite catalyst: synergetic effects of Fe₂O₃. *J Colloid Interface Sci.* 2019;539:135-145.
47. Yi YH, Li SK, Cui ZL, et al. Selective oxidation of CH₄ to CH₃OH through plasma catalysis: insights from catalyst characterization and chemical kinetics modelling. *Appl Catal Environ.* 2021;296:120384.
48. Yi YH, Wang X, Jafarzadeh A, et al. Plasma-catalytic ammonia reforming of methane over Cu-based catalysts for the production of HCN and H₂ at reduced temperature. *ACS Catal.* 2021;11(3):1765-1773.
49. Zhang QZ, Bogaerts A. Propagation of a plasma streamer in catalyst pores. *Plasma Sources Sci Technol.* 2018;27(3):035009.
50. Zhang QZ, Wang WZ, Bogaerts A. Importance of surface charging during plasma streamer propagation in catalyst pores. *Plasma Sources Sci Technol.* 2018;27(6):065009.
51. Wilson D, Langell MA. XPS analysis of oleylamine/oleic acid capped Fe₃O₄ nanoparticles as a function of temperature. *Appl Surf Sci.* 2014; 303:6-13.
52. Poulin S, França R, Moreau-Bélanger L, Sacher E. Confirmation of X-ray photoelectron spectroscopy peak attributions of nanoparticulate iron oxides, using symmetric peak component line shapes. *J Phys Chem C.* 2010;114(24):10711-10718.
53. Ma Z, Wang JF, Liu GF, et al. Regeneration of deactivated Fe₂O₃/Al₂O₃ oxygen carrier via alkali metal doping in chemical looping combustion. *Fuel Process Technol.* 2021;220:106902.
54. Jian YF, Yu TT, Jiang ZY, et al. In-depth understanding of the morphology effect of α-Fe₂O₃ on catalytic ethane destruction. *ACS Appl Mater Inter.* 2019;11:11369-11383.
55. Zhu J, Wang P, Zhang XB, et al. Dynamic structural evolution of iron catalysts involving competitive oxidation and carburization during CO₂ hydrogenation. *Sci Adv.* 2022;8(5):eabm3629.
56. Galindo-Hernández F, Domínguez JM, Portales B. Structural and textural properties of Fe₂O₃/γ-Al₂O₃ catalysts and their importance in the catalytic reforming of CH₄ with H₂S for hydrogen production. *J Power Sources.* 2015;287:13-24.
57. Kirchner J, Anollec JK, Lösch H, Kureti S. Methanation of CO₂ on iron based catalysts. *Appl Catal Environ.* 2018;223:47-59.
58. Liu Y, Murthy PR, Zhang X, Wang HY, Shi C. Phase transformation of iron oxide to carbide and Fe₃C as an active center for the RWGS reaction. *New J Chem.* 2021;45(47):22444-22449.
59. Bai SX, Shao Q, Feng YG, Bu LZ, Huang XQ. Highly efficient carbon dioxide hydrogenation to methanol catalyzed by zigzag platinum-cobalt nanowires. *Small.* 2017;13(22):1604311.
60. Yang B, Wang LJ, Hua ZL, Guo LM. How CO₂ chemisorption states affect hydrogenation activity. *Ind Eng Chem Res.* 2019;58(23):9838-9843.
61. Shirazi M, Neyts EC, Bogaerts A. DFT study of Ni-catalyzed plasma dry reforming of methane. *Appl Catal Environ.* 2017;205:605-614.
62. Xu SS, Chansai S, Xu SJ, et al. CO poisoning of Ru catalysts in CO₂ hydrogenation under thermal and plasma conditions: a combined kinetic and diffuse reflectance infrared Fourier transform spectroscopy-mass spectrometry study. *ACS Catal.* 2020;10(21): 12828-12840.
63. Zhao HB, Yu RF, Ma SC, et al. The role of Cu₁-O₃ species in single-atom Cu/ZrO₂ catalyst for CO₂ hydrogenation. *Nat Catal.* 2022;5(9): 818-831.
64. Yang CS, Pei CL, Luo R, et al. Strong electronic oxide-support interaction over In₂O₃/ZrO₂ for highly selective CO₂ hydrogenation to methanol. *J Am Chem Soc.* 2020;142(46):19523-19531.
65. Navarro-Jaen S, Navarro JC, Bobadilla LF, Centeno MA, Laguna OH, Odriozola JA. Size-tailored Ru nanoparticles deposited over γ-Al₂O₃ for the CO₂ methanation reaction. *Appl Surf Sci.* 2019;483:750-761.
66. Li JW, Dou LG, Liu YD, et al. One-step plasma reforming of CO₂-CH₄ into hydrogen and liquid fuels: the roles of Cu and Fe sites on products distribution. *Fuel Process Technol.* 2023;242:107648.
67. Ren YJ, Xin CY, Hao ZK, et al. Probing the reaction mechanism in CO₂ hydrogenation on bimetallic Ni/Cu(100) with near-ambient pressure X-ray photoelectron spectroscopy. *ACS Appl Mater Inter.* 2019; 12(2):2548-2554.

SUPPORTING INFORMATION

Additional supporting information can be found online in the Supporting Information section at the end of this article.

How to cite this article: Meng S, Wu L, Liu M, et al. Plasma-driven CO₂ hydrogenation to CH₃OH over Fe₂O₃/γ-Al₂O₃ catalyst. *AIChE J.* 2023;69(10):e18154. doi:10.1002/aic.18154